RESEARCH ARTICLE

HEART DISEASE

Immune-mediated denervation of the pineal gland underlies sleep disturbance in cardiac disease

Karin A. Ziegler[1,2], Andrea Ahles[1,2], Anne Dueck[1,2], Dena Esfandyari[1,2], Pauline Pichler[1], Karolin Weber[1], Stefan Kotschi[3], Alexander Bartelt[2,3,4,5], Inga Sinicina[6], Matthias Graw[6], Heinrich Leonhardt[7], Ludwig T. Weckbach[2,8,9], Steffen Massberg[2,8], Martina Schifferer[10,11], Mikael Simons[10,11,12], Luciano Hoeher[13], Jie Luo[13,14], Ali Ertürk[11,13,14], Gabriele G. Schiattarella[15,16,17], Yassine Sassi[18,19,20], Thomas Misgeld[10,11,12], Stefan Engelhardt[1,2]*

Disruption of the physiologic sleep-wake cycle and low melatonin levels frequently accompany cardiac disease, yet the underlying mechanism has remained enigmatic. Immunostaining of sympathetic axons in optically cleared pineal glands from humans and mice with cardiac disease revealed their substantial denervation compared with controls. Spatial, single-cell, nuclear, and bulk RNA sequencing traced this defect back to the superior cervical ganglia (SCG), which responded to cardiac disease with accumulation of inflammatory macrophages, fibrosis, and the selective loss of pineal gland–innervating neurons. Depletion of macrophages in the SCG prevented disease-associated denervation of the pineal gland and restored physiological melatonin secretion. Our data identify the mechanism by which diurnal rhythmicity in cardiac disease is disturbed and suggest a target for therapeutic intervention.

In healthy humans, the sleep-wake cycle is tightly controlled by the daytime-dependent diurnal secretion of melatonin that achieves synchrony with Earth's 24-hour day and night (diurnal) cycle (*1*–*3*). Melatonin synthesis occurs in the pineal gland and is, together with its secretion, tightly controlled by sympathetic neurons that project from the superior cervical ganglia (SCG). In addition to pineal gland–innervating neurons (*4*), the SCG harbors heart-innervating neurons (*5*, *6*). The end organ–innervating neurons in the SCG receive input from central sympathetic nuclei (*7*). In heart disease, low melatonin levels and disruptions of sleep-wake rhythmicity frequently occur (*8*–*10*). These disruptions considerably contribute to the overall disease burden, yet there is no consensus as to their treatment (*11*). The mechanism underlying the altered sleep-wake cycle in cardiac disease has remained elusive, and the role of pineal gland innervation has not been addressed. In this work, we systematically charted the pineal gland–controlling neuronal circuits in cardiac disease. Our results indicate severe and likely irreversible immune-mediated destruction of a specific subset of sympathetic neurons that control diurnal rhythmicity of pineal melatonin. These data reveal that defective sympathetic control of the pineal gland underlies the disturbance of diurnal rhythmicity in cardiac disease.

Cardiac disease causes sympathetic denervation and dysfunction of the pineal gland

The pineal gland and its peripheral sympathetic regulation (*12*) play a key role in diurnal rhythms. Additionally, both diurnal (*9*) and sympathetic disruptions (*13*) are highly prevalent in chronic cardiac disease. Thus, we hypothesized that in such pathological settings, the neuronal control of pineal gland function might be impaired. To test this hypothesis, we assessed pineal gland sympathetic innervation in humans with cardiac disease compared with heart-healthy controls. We collected postmortem pineal glands from seven heart disease patients and nine heart-healthy controls, performed tissue clearing, and stained them for the sympathetic marker enzyme tyrosine hydroxylase. In pineal gland tissue from the patients with cardiac disease, we observed a significant reduction of axonal density (Fig. 1, A and B). We reasoned that this loss of innervation of the pineal gland could provide an explanation for the lower melatonin levels observed in humans with cardiac disease (*14*) and therefore sought to investigate the underlying cellular mechanism in an animal model of cardiac disease. We surveyed pineal gland function in mice subjected to transverse aortic constriction (TAC) to exert left ventricular pressure overload, a condition that leads to pathologic cardiac hypertrophy and failure (Fig. 1, C to F, and fig. S1, A and B) (*15*). Plasma melatonin concentrations in these TAC-treated mice were reduced, relative to controls, 4 weeks after the respective intervention (Fig. 1D). We then asked whether this change in pineal gland function caused alterations of a comprehensive standard set of parameters for diurnal rhythmicity, including respirometry to survey metabolic rates, nutrient uptake, body mass, and activity (determined with infrared arrays). We found a marked disruption of diurnal rhythmicity with a reduced amplitude in TAC mice compared with controls. This relative loss of diurnal rhythmicity was not associated with changes in total energy expenditure or activity, which indicates that the shift in cycling is a specific effect rather than being related to unspecific sickness of TAC mice (Fig. 1, E and F).

Mice allow the genetic labeling of sympathetic neurons with superior signal-to-noise ratio axon imaging (*16*). We next sought to generate mice with fluorescently labeled sympathetic axons by cross breeding dopamine-β-hydroxylase (Dbh)–Cre mice with tdTomato^{flox} mice (fig. S1C). Application of cardiac pressure overload for 4 weeks recapitulated the hallmarks of pineal gland pathology observed in humans with chronic cardiac disease, namely a significantly lower sympathetic axonal density compared with sham-operated animals (Fig. 1, G and H, and fig. S1D). We observed similar effects of pineal gland denervation (Fig. 1, I and J) in another disease model: heart failure with preserved ejection fraction (HFpEF) induced by chronic metabolic and hypertensive stress (*17*). Pineal gland cellular composition (fig. S1E) as well as pineal gland area (fig. S1F) remained unchanged, prompting us to analyze next the SCG from which the pineal gland–innervating axons originate.

[1]Institute of Pharmacology and Toxicology, Technical University Munich (TUM), Munich, Germany. [2]DZHK (German Centre for Cardiovascular Research), Partner Site Munich Heart Alliance, Munich, Germany. [3]Institute for Cardiovascular Prevention (IPEK), Faculty of Medicine, Ludwig-Maximilians-Universität (LMU) München, Munich, Germany. [4]Institute for Diabetes and Cancer, Helmholtz Center Munich, Neuherberg, Germany. [5]Department of Molecular Metabolism & Sabri Ülker Center for Metabolic Research, Harvard. T.H. Chan School of Public Health, Boston, MA, USA. [6]Institute of Legal Medicine, Faculty of Medicine, Ludwig-Maximilians-Universität (LMU) München, Munich, Germany. [7]Human Biology & Bioimaging, Faculty of Biology, Ludwig-Maximilians-Universität (LMU) München, Munich, Germany. [8]Medizinische Klinik und Poliklinik I, Klinikum der Universität München, Munich, Germany. [9]Institute of Cardiovascular Physiology and Pathophysiology, Biomedical Center, Ludwig-Maximilians-Universität (LMU), Planegg-Martinsried, Germany. [10]DZNE (German Center for Neurodegenerative Diseases), Munich, Germany. [11]Munich Cluster for Systems Neurology (SyNergy), Munich, Germany. [12]Institute of Neuronal Cell Biology, Technical University Munich (TUM), Munich, Germany. [13]Institute for Tissue Engineering and Regenerative Medicine (iTERM), Helmholtz Center Munich, Neuherberg, Germany. [14]Institute for Stroke and Dementia Research, Klinikum der Universität München, Ludwig-Maximilians-Universität (LMU) München, Munich, Germany. [15]DZHK (German Centre for Cardiovascular Research), Partner Site Berlin, Berlin, Germany. [16]Max Rubner Center for Cardiovascular Metabolic Renal Research (MRC), Deutsches Herzzentrum der Charité (DHZC), Charité-Universitätsmedizin Berlin, Berlin, Germany. [17]Translational Approaches in Heart Failure and Cardiometabolic Disease, Max Delbrück Center for Molecular Medicine in the Helmholtz Association (MDC), Berlin, Germany. [18]Fralin Biomedical Research Institute at Virginia Tech Carilion, Roanoke, VA, USA. [19]Department of Biomedical Sciences and Pathobiology, Virginia-Maryland College of Veterinary Medicine, Virginia Tech, Blacksburg, VA, USA. [20]Department of Internal Medicine, Virginia Tech Carilion School of Medicine, Roanoke, VA, USA.
*Corresponding author. Email: stefan.engelhardt@tum.de

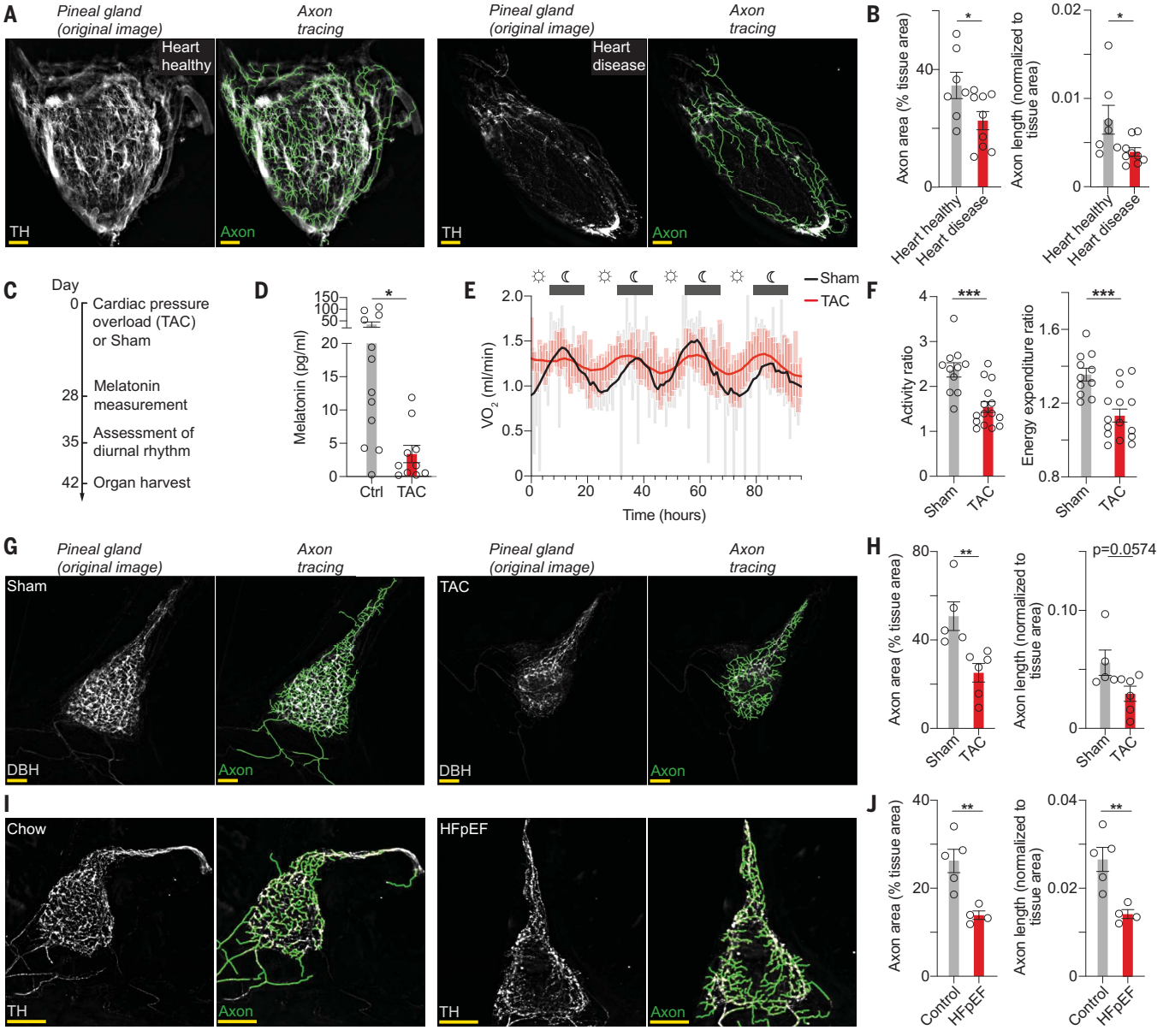

Fig. 1. Cardiac disease causes sympathetic denervation and dysfunction of the pineal gland. (**A**) Representative images of human pineal glands after clearing and staining for tyrosine hydroxylase (TH). Scale bar, 1 mm. (**B**) Quantification of axon area and length. Axonal parameters were normalized to pineal gland area. (**C**) Timeline of mouse behavioral study. (**D**) Measurement of melatonin in plasma from C3H/HeJ mice 28 days after the respective intervention. (**E** and **F**) Assessment of diurnal rhythm in C3H/HeJ mice after sham and TAC. Mouse behavior including metabolic measurements [including oxygen consumption (VO_2) and energy expenditure] as well as activity (beam breaks per minute) was continuously recorded. The ratio between dark and light was calculated for activity and energy expenditure (kcal per hour). (**G**) Representative images of mouse pineal glands from dopamine β-hydroxylase (DBH) Cre/tdTomato^{flox} mice 28 days after sham and TAC. Scale bar, 200 μm. (**H**) Quantification of axon area and length. Axonal parameters were normalized to pineal gland area. (**I**) Representative images of mouse pineal glands stained for TH 15 weeks after control (chow) and HFpEF treatment. Scale bar, 200 μm. (**J**) Quantification of axon area and length. Axonal parameters were normalized to pineal gland area. Data are mean ± SEM of n = 7 specimens (heart healthy) and n = 9 (heart disease) for (A) and (B); n = 12 mice (sham), and n = 10 (TAC) for (D); n = 11 (sham) and n = 15 (TAC) for (E) and (F); and n = 5 (sham), n = 6 (TAC), n = 5 (chow), and n = 4 (HFpEF) for (G) to (J). Statistical analysis was performed using Student's t test. *P < 0.05, **P < 0.01, ***P < 0.001.

Chronic cardiac disease causes fibrotic scarring and hypertrophy of SCG in mice and humans

Morphometry and histopathology of SCG derived from mice subjected to TAC revealed significant hypertrophy with significantly higher ganglionic volumes (Fig. 2, A and B). SCG from TAC mice further showed extensive fibrotic scarring when compared with that of sham-operated animals, which suggests massive, possibly irreversible organ damage (Fig. 2, A and B).

We then asked whether these findings can be translated to chronic cardiac disease in humans and prospectively obtained a total of 38 SCG specimens from 19 individuals with or without heart disease upon autopsy (table S1). As in mice with cardiac disease, SCG from patients with heart disease were significantly enlarged and exhibited increased interstitial scarring, with the stained matrix volume amounting to ~70% of total intraganglionic volume

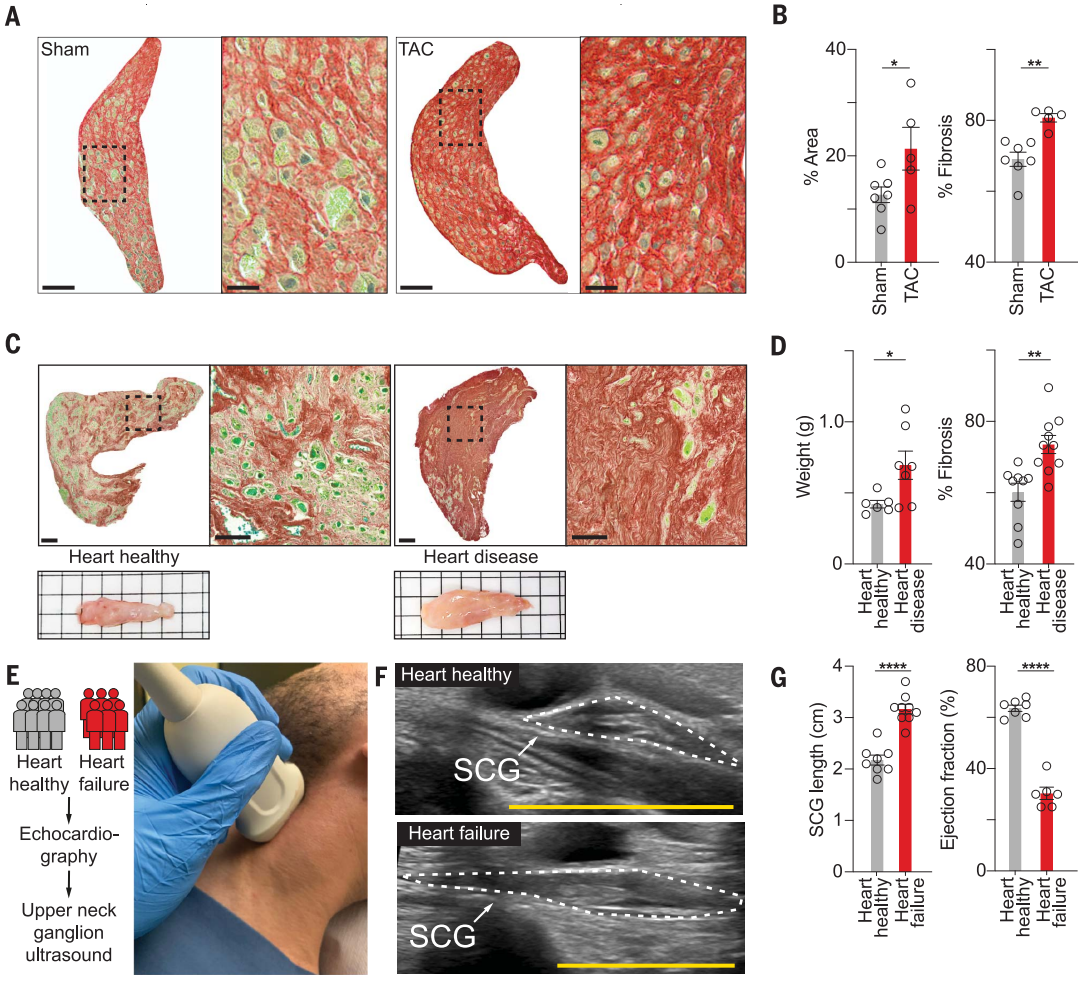

Fig. 2. Chronic cardiac disease causes fibrotic scarring and hypertrophy of SCG in mice and humans. (**A**) (Left) Representative images of mouse superior cervical ganglia 42 days after sham and TAC surgery stained with Fast Green and Sirius Red. Scale bar, 200 μm. (Right) Magnified images of the boxed regions. Scale bar, 50 μm. (**B**) Quantification of SCG area and fibrosis. (**C**) (Top left) Paraffin sections stained with Fast Green and Sirius Red. Scale bar, 500 μm. The boxes indicate the region of the magnified images. (Top right) Magnification of the boxed regions. Scale bar, 200 μm. (Bottom) Representative images of superior cervical ganglia from individuals with and without heart disease. (**D**) Quantification of SCG weight and Sirius Red$^+$ area in transverse SCG sections. (**E** to **G**) Evaluation of SCG morphometry in a prospective clinical study. (E) (Left) Workflow of the clinical study. (Right) Exemplary setup of an SCG ultrasound examination. (F) Representative images from human SCG acquired by ultrasound (top, healthy; bottom, heart failure). Scale bar, 3.5 cm. (G) Quantification of SCG length and ejection fraction. Data are mean ± SEM of $n = 7$ mice (sham) and $n = 5$ (TAC) for (A) and (B); $n = 6$ (heart healthy) and $n = 7$ (heart disease) for (D); $n = 9$ (heart healthy) and $n = 10$ (heart disease) for (C); $n = 7$ to 8 study participants (heart healthy) and $n = 6$ to 9 (heart failure) for (E) to (G). Statistical analysis was performed using Student's t test. *$P < 0.05$, **$P < 0.01$, ****$P < 0.0001$.

(Fig. 2, C and D). The extent of ganglionic fibrosis significantly correlated with the extent of myocardial remodeling (fig. S2A).

The degree of SCG hypertrophy led us to hypothesize that the size of the SCG may serve as an imaging biomarker for heart failure. In a clinical study, we therefore prospectively evaluated SCG dimensions with quantitative ultrasound imaging in patients with heart failure and healthy controls (Fig. 2, E and F, fig. S2B, and tables S2 and S3). Evaluation with current clinical ultrasound equipment revealed a significant increase of SCG dimensions in patients with heart failure (Fig. 2G), with eight out of nine patients displaying a ~150% higher SCG length. We observed a significant correlation between SCG size and ejection fraction (fig. S2C), which is consistent with functional interdependence.

Heart disease triggers macrophage infiltration and loss of pineal gland–innervating neurons in SCG

To dissect and quantitatively assess the cellular basis for the histomorphologic alterations of the SCG, we performed single-cell and single-nuclei RNA sequencing (scRNA-seq and snRNA-seq, respectively). Ganglia were isolated from control mice and mice that had been subjected to TAC (Fig. 3A). In total, 20,780 cells passed the quality control and were used as input for computational analysis. The cellular compendium comprised five major cell types: sympathetic neurons, Schwann cells, fibroblasts, endothelial cells, and immune cells (Fig. 3A and fig. S3A). snRNA-seq furthermore identified two distinct cell clusters among the sympathetic neurons, the smaller of which selectively expressed melatonin receptor 1A (*Mtnr1a*). We assigned this *Mtnr1a*$^+$ neuronal cell cluster as bona fide pineal gland–innervating neurons, because the target organs of sympathetic innervation typically secrete specific guidance cues that allow for selective axon growth during embryonic development and hence, specific innervation (*18*, *19*) (Fig. 3, A and B, and fig. S3A). We cannot exclude, however, that further neuronal populations or subpopulations exist within the SCG, which may exert additional specific functions, and that further subpopulations besides *Mtnr1a*$^+$ cells contribute to pineal gland innervation. All neurons share typical markers for sympathetic neurons—including tyrosine hydroxylase (*Th*), dopamine-β-hydroxylase (*Dbh*), neuropeptide Y (*Npy*), peripherin (*Prph*), and synapsin II (*Syn2*)—in line with reports of cell inventories of other sympathetic ganglia (*7*, *20*). Pineal gland–innervating neurons were, in addition to *Mtnr1a*, characterized by expression of small nucleolar RNA host gene 11 (*Snhg11*), Ankyrin 2 (*Ank2*), Hand2 opposite strand 1 (*Hand2os1*), Semaphorin 6D (*Sema6d*), EPH Receptor A5 (*Epha5*), neuronal cell adhesion molecule (*Nrcam*), synaptosome associated protein 91 (*Snap91*), and calcium voltage-gated channel subunit α1 A (*Cacna1a*) (Fig. 3B and fig. S3A). Although we found consistent expression for *Cacna1a* mRNA, this may not translate to functional calcium current (*21*). After Schwann cells, a high number of immune cells were also detected within the SCG, most of which were macrophages (5 to 8% in scSeq) (fig. S3, B to F). Spatial sequencing (MERSCOPE platform, Vizgen) of cryosections prepared from mouse SCG by using 140 RNA probes allowed transcriptome mapping

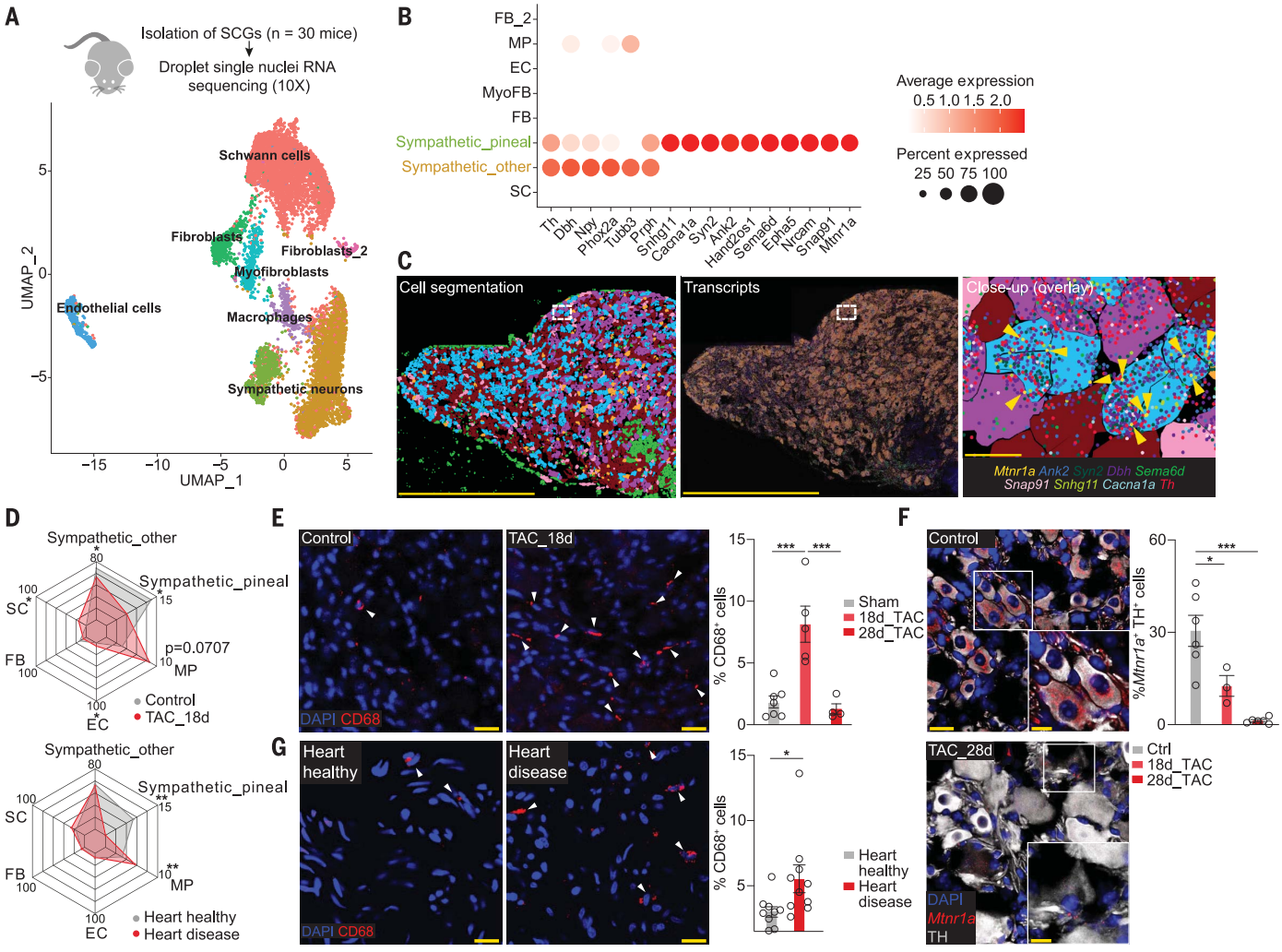

Fig. 3. Heart disease triggers macrophage infiltration and loss of pineal gland–innervating neurons in SCG. (**A**) UMAP projection of 9172 cellular nuclei from SCG isolated 5 days after sham and TAC. (**B**) Dot plot of neuron subtype–specific genes in single-nuclei sequencing. (**C**) SCG cell segmentation (left) and transcriptional profile (middle) assessed with spatial RNA sequencing. (Right) Representative area in high magnification. Overlay shows the merging of cell segmentation and neuron cluster–defining marker genes. Scale bar, 1 mm (magnification, 25 μm). (**D**) Quantitative assessment of cellular composition in (top) mouse and (bottom) human SCG by means of genetic deconvolution of RNA sequencing libraries (percent of relative fraction). (**E**) $CD68^+$ cells (arrows) in the respective ganglia with quantification. Scale bar, 20 μm. (**F**) In situ hybridization and immunofluorescence assays in mouse superior cervical ganglia with quantification. The boxes indicate the region of the close-up images. Scale bar, 20 μm (magnification, 10 μm). (**G**) $CD68^+$ cells (arrows) in the respective ganglia with quantification. Scale bar, 20 μm. Data are from $n = 4$ mice (control) and $n = 3$ (TAC) for (D); $n = 7$ (sham), $n = 5$ [TAC_d18 (day 18)], and $n = 4$ [TAC_d28 (day 28)] for (E); $n = 6$ (control and TAC_d28) and $n = 3$ (TAC_d18) for (F); $n = 3$ specimens (heart healthy and heart disease) for (D); $n = 9$ (heart healthy) and $n = 10$ (heart disease) for (G). Student's t test was applied for (D) and (G), and one-way ANOVA with Bonferroni's post-hoc test was applied for statistical analysis of (E) and (F). $^*P < 0.05$, $^{**}P < 0.01$, $^{***}P < 0.001$. FB, fibroblasts; MyoFB, myofibroblasts; MP, macrophages; EC, endothelial cells; sympathetic_pineal, pineal gland–innervating sympathetic neurons; sympathetic_other, sympathetic neurons innervating other organs; SC, Schwann cells.

with single-cell resolution (Fig. 3C and fig. S4). Automated, machine learning–based cell segmentation combined with unsupervised transcriptome-based UMAP (uniform manifold approximation and projection) clustering yielded six distinct cell clusters, including two major subclusters of sympathetic neurons (Fig. 3C and fig. S4B). One cluster expressed a set of marker genes highly similar to the bona fide pineal gland–innervating neurons identified by snSeq (Fig. 3B). The staining of the entire sympathetic nervous system in optically cleared intact adult mice allowed us to generate a three-dimensional dataset of sympathetic innervation, which permitted the uninterrupted tracing of the sympathetic innervation originating from the SCG, through the upper neck, into the cranial cavity, and all the way to the pineal gland (movie S1). These axons exclusively originated from the cranial pole of the SCG, which is in line with the cranial positioning of the respective neurons (fig. S4B).

We then determined a set of marker genes for the major cell populations in the SCG, which enabled the genetic deconvolution (*22*) of deep RNA-seq data of mouse and human ganglia (fig. S5A). Ganglia from mice that had been subjected to TAC displayed a marked increase of the macrophage cell fraction and a significant reduction of sympathetic pineal gland–innervating neurons (sympathetic_pineal) (Fig. 3D) at day 18 after the procedure, well before decompensated heart failure was fully established (day 28) (fig. S5B). To independently validate the findings of changes in cellular composition, we antibody-stained tissue cryosections of SCG obtained from TAC-subjected or control mice for the macrophage marker CD68 (Fig. 3E) and probed for mRNA expression of

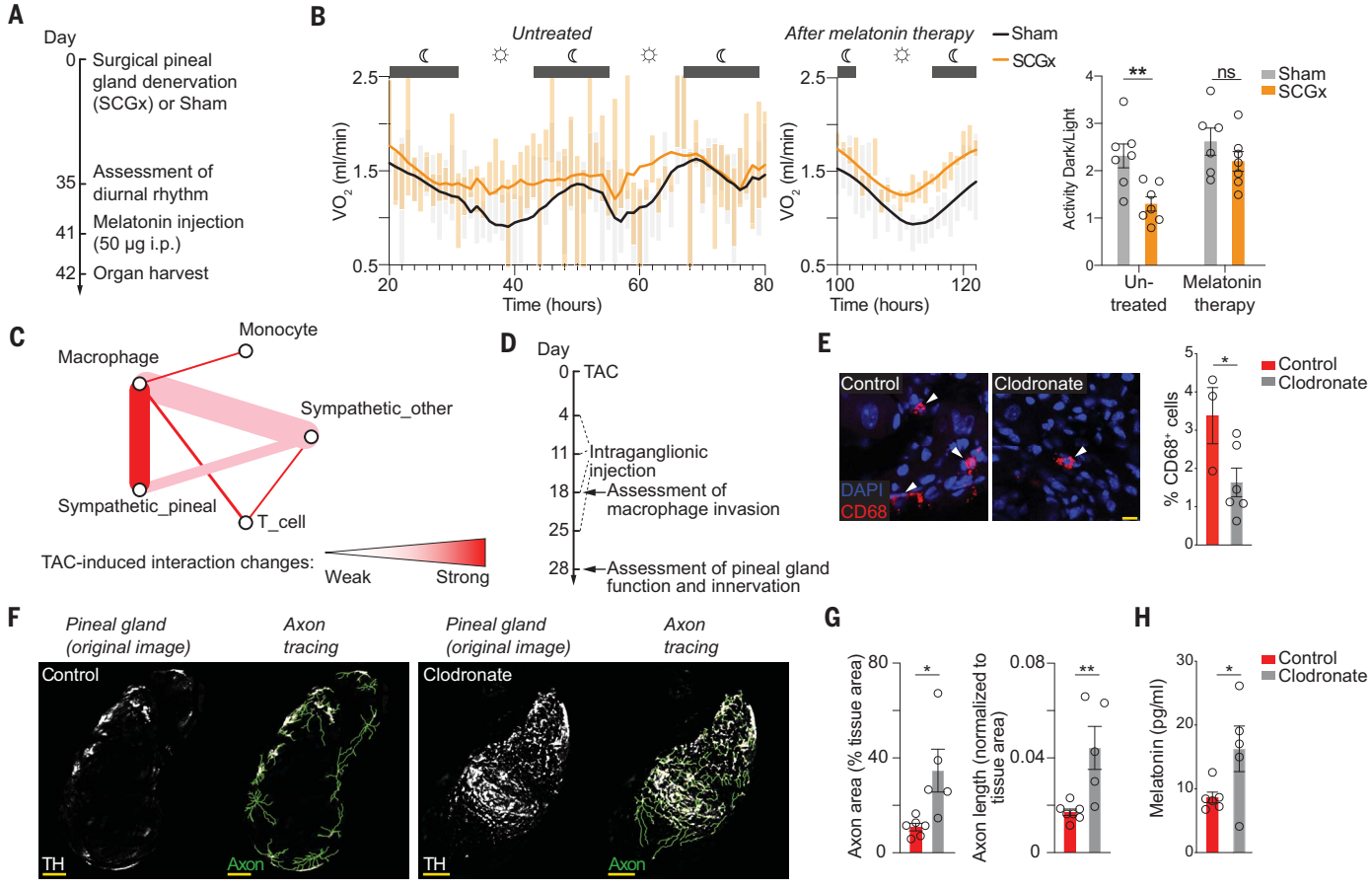

Fig. 4. Local clodronate injection attenuates pineal gland denervation and dysfunction. (**A** and **B**) Assessment of diurnal rhythm in C3H/HeJ mice after sham and SCGx. "Untreated" refers to the time period before melatonin injection. (A) Timeline of the study. From day 35 on, mouse behavior including oxygen consumption (VO_2) and activity (beam breaks per minute) was continuously recorded. After 6 days of recording, 50 µg melatonin was once injected intraperitoneally at the time of physiological peak of endogenous melatonin production. (B) (Right) The dark-light ratio was calculated for activity. (**C**) Neuroimmune interaction map in superior cervical ganglia generated through intercellular ligand-receptor interaction (iTALK R package) from single-cell SCG transcriptomes. Relative differences of ligand-receptor pairs between sham and 5 days after TAC. The color indicates the acute TAC-induced changes in ligand-receptor pairings: white indicates weak, pink indicates moderate, and red indicates strong changes. (**D**) Timeline of clodronate experiments. (**E**) $CD68^+$ cells (arrows) in the respective ganglia with quantification. Scale bar, 10 µm. (**F**) Representative images of mouse pineal glands stained for tyrosine hydroxylase (TH). Scale bar, 100 µm. (**G**) Quantification of axon area and length normalized to pineal gland area. (**H**) Measurement of melatonin in plasma from C3H/HeJ mice 28 days after the respective intervention. Data are means ± SEM of n = 6 to 7 mice for (A) and (B), n = 3 (TAC control, day 18) and n = 6 (TAC clodronate, day 18) for (E), and n = 6 to 7 (TAC control, day 28) and n = 5 (TAC clodronate, day 28) for (G) and (H). Student's t test was applied for statistical analysis of (E), (G), and (H). Two-way ANOVA with Bonferroni's post-hoc test was applied for statistical analysis of (B). $^*P < 0.05$, $^{**}P < 0.01$.

the sympathetic pineal gland–innervating neuronal cell marker gene *Mtnr1a* using in situ hybridization (Fig. 3F). Quantitative analysis confirmed a significant increase of $CD68^+$ macrophages and a significant loss of $Mtnr1a^+$ neurons (Fig. 3, E and F). We did not observe macrophage accumulation in non–cardiac-innervating ganglia (fig. S5D) or elevated levels of general inflammation markers (fig. S5E).

The loss of sympathetic pineal gland–innervating neurons was already significant 18 days after TAC and rapidly progressed toward an almost entire loss of $Mtnr1a^+$ neurons (Fig. 3F). Electron microscopy that we performed 28 days after TAC corroborated signs of axonal damage in SCG neurons, which was indicated by electron-dense alterations predominantly localized at the axon initiation segment (AIS) (fig. S6). These alterations at the AIS were predominantly found in large but not small neurons, which suggests that pineal gland–innervating neurons were affected by AIS darkening (*23*).

Transcriptome analysis of human SCG autopsy samples from patients with established cardiac disease recapitulated a significant macrophage infiltration (albeit to a lesser extent at this late stage of cardiac disease) and the loss of sympathetic pineal gland–innervating neurons (Fig. 3D). In addition, immunofluorescent detection of intraganglionic macrophages in these samples confirmed their disease-associated accumulation (Fig. 3G).

Local clodronate injection attenuates pineal gland denervation and dysfunction

We next sought to assess the effects of pineal gland denervation on melatonin-related diurnal rhythmicity. Pineal gland denervation was achieved by means of bilateral, surgical removal of the SCG (SCGx) and diurnal rhythmicity was assessed with continuous recording of activity and respiration by indirect calorimetry (Fig. 4, A and B). SCGx resulted in a marked disruption of diurnal rhythm (Fig. 4B). Diurnal rhythmicity, however, could be completely restored by supplementation of melatonin (Fig. 4B). The observed infiltration of the SCG by macrophages and the concomitant loss of sympathetic pineal gland–innervating neurons prompted us to speculate that these

findings might be related. To this end, we mapped intercellular communication in SCG by means of transcriptome profiling (*24*). At early stages of cardiac disease (5 days after TAC), the most pronounced alterations occurred in the communication network between macrophages and sympathetic pineal gland–innervating neurons (Fig. 4C). We then aimed to specifically interfere with the presumed detrimental macrophage-neuron interaction and to deplete macrophages locally in the SCG in TAC-treated mice (Figs. 4, D to H). Mice were subjected to TAC, which was followed by weekly intraganglionic injections of the macrophage inhibitor clodronate. The SCG of the clodronate-injected mice exhibited significant depletion of macrophages (Fig. 4E). Local clodronate injection into the SCG prevented pineal gland denervation and dysfunction, as indicated by increased sympathetic axonal density within the pineal gland and significantly increased melatonin levels (Fig. 4, F to H).

We then asked whether the detrimental macrophage-neuron interaction could in principle be recapitulated in a defined ex vivo system or whether other cell types are necessary for this interaction. Coculture of sympathetic neurons with proinflammatory ("M1-like") but not with control macrophages inhibited neurite outgrowth and induced cell loss of nicotine-stimulated but not of quiescent sympathetic neurons (fig. S7, A to E). Treatment with cobra venom factor (CVF), a broad-spectrum complement inhibitor that blocks macrophage activation (*25*), effectively prevented both neuronal cell loss and rescued neurite outgrowth in this setting (fig. S7, B and C). Thus, activated macrophages play a central role in sympathetic neuron cell death, and local macrophage inhibition may prove to be therapeutically effective.

Discussion

Disruption of the sleep-wake pattern and melatonin secretion is an established consequence of cardiac disease, yet the underlying mechanism has remained elusive. This study identifies sympathetic denervation of the pineal gland as the underlying cause and suggests a means for therapeutic intervention.

The fibrotic remodeling and the loss of neurons appear to be specific for the SCG with milder abnormalities such as neuronal hypertrophy (a typical sign of their chronic overactivation) in the stellate ganglion and adrenal medulla (fig. S5C) (*26*). Our coculture experiments suggested that the simultaneous occurrence of inflammatory macrophage polarization and chronic activation of sympathetic neurons initiated ganglionic disease. This suggests that the discriminating factor in the SCG is the extent of the inflammatory response and/or its macrophage-dominated nature compared with that of other ganglia. This would also be compatible with reports on the stellate ganglion, where mainly T cell infiltration (and, to a much lesser extent, macrophage infiltration) was observed in cardiac disease (*27*–*29*).

Our findings call for further studies to elucidate the mechanisms that trigger macrophage infiltration and their activation in the SCG. These further studies should include analyses of the relative roles of cardiac afferent and spinal preganglionic projections and CXCL2, IL1A, and TNFA, recruitment and activation factors previously reported for neuron-associated macrophages (*16*).

Concerning the clinical problem of sleep disturbances in cardiac disease, our data call for the exploration of ganglion-targeted therapeutic modalities. Such an anti-inflammatory intervention could be local and minimally invasive and may prevent irreversible damage of autonomic ganglion structure and function. In those patients in whom such damage is manifested, the supplementation of melatonin should be investigated in systematic clinical trials to further extend the current limited evidence (*30*). Our findings on the pronounced hypertrophy of the SCG as detected by ultrasound call for a prospective study with serial follow-ups to determine whether this simple and robust biomarker can identify cardiac patients who are at risk for imminent pineal denervation and are therefore candidates for therapeutic and preventive intervention.

Our study suggests a paradigm in which cardiac disease affects an anatomically distant organ and that stems from the spatial integration of organ-specific neuronal subpopulations in sympathetic ganglia (fig. S8). Beyond its implications for cardiac disease, the role of sympathetic ganglia as relay stations between organs warrants further exploration with regard to other disease entities.

REFERENCES AND NOTES

1. R. S. Edgar *et al*., *Nature* **485**, 459–464 (2012).
2. J. C. Dunlap, *Cell* **96**, 271–290 (1999).
3. H. J. Lynch, R. J. Wurtman, M. A. Moskowitz, M. C. Archer, M. H. Ho, *Science* **187**, 169–171 (1975).
4. C. W. Bowers, L. M. Dahm, R. E. Zigmond, *Neuroscience* **13**, 87–96 (1984).
5. A. M. D. Végh *et al*., *J. Cardiovasc. Dev. Dis.* **3**, 28 (2016).
6. K. A. Ziegler *et al*., *Cardiovasc. Res.* **114**, 291–299 (2018).
7. A. Furlan *et al*., *Nat. Neurosci.* **19**, 1331–1340 (2016).
8. S. T. Anderson, G. A. FitzGerald, *Science* **369**, 1164–1165 (2020).
9. S. S. Thosar, M. P. Butler, S. A. Shea, *J. Clin. Invest.* **128**, 2157–2167 (2018).
10. B. M. Kuehn, *Circulation* **134**, 1907–1908 (2016).
11. I. García-Lunar, V. Fuster, B. Ibanez, *Eur. Heart J.* **42**, 2100–2102 (2021).
12. J. Axelrod, *Science* **184**, 1341–1348 (1974).
13. E. N. Bardsley, D. J. Paterson, *J. Physiol.* **598**, 2957–2976 (2018).
14. P. Brugger, W. Marktl, M. Herold, *Lancet* **345**, 1408 (1995).
15. H. A. Rockman *et al*., *Proc. Natl. Acad. Sci. U.S.A.* **88**, 8277–8281 (1991).
16. R. M. Pirzgalska *et al*., *Nat. Med.* **23**, 1309–1318 (2017).
17. G. G. Schiattarella *et al*., *Nature* **568**, 351–356 (2019).
18. S. Cho *et al*., *Proc. Natl. Acad. Sci. U.S.A.* **93**, 2862–2866 (1996).
19. E. Scott-Solomon, E. Boehm, R. Kuruvilla, *Nat. Rev. Neurosci.* **22**, 685–702 (2021).
20. A. Zeisel *et al*., *Cell* **174**, 999–1014.e22 (2018).
21. I. M. Mintz, M. E. Adams, B. P. Bean, *Neuron* **9**, 85–95 (2005).
22. A. M. Newman *et al*., *Nat. Methods* **12**, 453–457 (2015).
23. J. I. Luebke, L. L. Wright, *Brain Res.* **589**, 1–14 (1992).
24. M. Efremova, M. Vento-Tormo, S. A. Teichmann, R. Vento-Tormo, *Nat. Protoc.* **15**, 1484–1506 (2020).
25. S. Z. Wang, Z. H. Qin, *Toxins (Basel)* **10**, 100 (2018).
26. O. A. Ajijola *et al*., *Circ. Arrhythm. Electrophysiol.* **5**, 1010–1116 (2012).
27. O. A. Ajijola *et al*., *JCI Insight* **2**, e94715 (2017).
28. D. Zhang *et al*., *Basic Res. Cardiol.* **116**, 28 (2021).
29. S. Rizzo *et al*., *Circ. Arrhythm. Electrophysiol.* **7**, 224–229 (2014).
30. H. Sun, A. M. Gusdon, S. Qu, *Curr. Opin. Lipidol.* **27**, 408–413 (2016).

ACKNOWLEDGMENTS

We thank J. Auerswald and A. Bomhard for the microsurgical interventions; J. Decker, S. Brummer, L. Koblitz, and R. Wallace for excellent technical assistance; H. Jodeleit for help with diurnal rhythm studies; T. Hasenbein for excellent help with the Python-based analysis of spatial RNA seq data; B. Laggerbauer for critical reading of the manuscript; and A. Verschoor and C. Schulz for advice. **Funding:** K.A.Z. was supported by the German Cardiac Society (research grant) and by TUM (stipend by PhD program in Medical Life Science and Technology). A.B. was supported the European Research Council Starting Grant Proteofit. A.D. and S.E. are supported by the Deutsche Forschungsgemeinschaft (DFG, German Research Foundation) (project ID 403584255–TRR 267). A.D., D.E., A.B., S.M., and S.E. are supported in the framework of the DZHK and its partner site, Munich Heart Alliance (MHA). G.G.S. is supported by grants from the DZHK (German Centre for Cardiovascular Research) and the DFG (SFB-1470 – A02). Work in T.M.'s lab is supported by the DFG through TRR 274/1 B03/ C02-ID 408885537; Mi 694/7-1, 8-1, and 9-1 (FOR ImmunoStroke A03-ID 428663564); the Munich Center for Systems Neurology (SyNergy EXC 2145-ID 390857198); the ERC under the European Union's Seventh Framework Program (FP/2007-2013, ERC grant agreement no. 616791); and the German Center for Neurodegenerative Diseases (DZNE). M.S. is also supported by the DFG through TRR 274/1 Z0-ID 408885537 and SyNergy EXC 2145-ID 390857198. S.E. was supported by the DFG through Research Training Group GRK2338 and by the BMBF in the framework of the Cluster4future program (CNATM - Cluster for Nucleic Acid Therapeutics Munich). **Author contributions:** Initiation and conceptualization: K.A.Z. and S.E.; Methodology: K.A.Z., A.A., A.D., P.P., K.W., S.K., A.B., L.T.W., T.M., S.M.,and M.Sch.; Investigation: K.A.Z., A.D., D.E., L.T.W., M.Sch., and G.G.S.; Writing – Original draft: K.A.Z.; Writing – editing: S.E. with input from all authors; Visualization: K.A.Z. and S.E.; Supervision: T.M., S.M., and S.E.; Project administration: K.A.Z.; Funding acquisition: K.A.Z. and S.E. **Competing interests:** The TU Munich has filed a patent related to local modulation of macrophages in sympathetic ganglia for which K.A.Z. and S.E. are listed as inventors. **Data and materials availability:** All data are available in the main text or the supplementary materials. Single-cell, single-nucleus, spatial, and bulk RNA-sequencing files can be accessed with the NCBI's Gene Expression Omnibus (accession no. GSE231767).

SUPPLEMENTARY MATERIALS

science.org/doi/10.1126/science.abn6366
Materials and Methods
Figs. S1 to S8
Tables S1 to S4
References (*31*–*41*)
Movie S1
MDAR Reproducibility Checklist

Submitted 10 December 2021; resubmitted 22 December 2022
Accepted 1 June 2023
10.1126/science.abn6366